CrossMark

Nanoflare Heating of the Solar Corona Observed in X-Rays

Vishal Upendran[1] , Durgesh Tripathi[1] , N. P. S. Mithun[2] , Santosh Vadawale[2] , and Anil Bhardwaj[2]
[1] Inter-University Centre for Astronomy and Astrophysics, Pune, 411007, India; uvishal@iucaa.in
[2] Physical Research Laboratory, Navrangpura, Ahmedabad, Gujarat 380 009, India

Abstract

The existence of the million-degree corona above the cooler photosphere is an unsolved problem in astrophysics. Detailed study of the quiescent corona that exists regardless of the phase of the solar cycle may provide fruitful hints toward resolving this conundrum. However, the properties of heating mechanisms can be obtained only statistically in these regions due to their unresolved nature. Here, we develop a two-step inversion scheme based on the machine-learning scheme of Upendran & Tripathi (2021a) for the empirical impulsive heating model of Pauluhn & Solanki (2007), and apply it to disk integrated flux measurements of the quiet corona as measured by the X-ray solar monitor on board Chandrayaan-2. We use data in three energy passbands, viz, 1–1.3, 1.3–2.3, and 1–2.3 keV, and estimate the typical impulsive event frequencies, timescales, amplitudes, and the distribution of amplitudes. We find that the impulsive events occur at a frequency of $\approx$25 events per minute with a typical lifetime of $\approx$10 minutes. They are characterized by a power-law distribution with a slope $\alpha \leqslant 2.0$. The typical amplitudes of these events lie in an energy range of 10^{21}–10^{24} erg, with a typical radiative loss of about $\approx 10^{3}$ erg cm^{-2} s^{-1} in the energy range of 1–2.3 keV. These results provide further constraints on the properties of subpixel impulsive events in maintaining the quiet solar corona.

Unified Astronomy Thesaurus concepts: Quiet solar corona (1992); Solar coronal heating (1989); Solar x-ray emission (1536); Convolutional neural networks (1938)

1. Introduction

The anomalous heating of the solar corona occurs not just in bright active regions, but also in the quiet Sun (QS) regions. Hence, the route to understanding the temperature of the corona begins by understanding the heating in QS. The two predominant physical mechanisms responsible for heating the solar corona are through dissipation of magnetohydrodynamic (MHD) waves via resonant absorption or phase mixing (see, e.g., Alfvén & Lindblad 1947; Osterbrock 1961; Antolin et al. 2008) or that of magnetic stresses via magnetic reconnection or Joule heating (see, e.g., Parker 1972; Chiueh & Zweibel 1987; Parker 1988; Hansteen et al. 2010, and also Klimchuk 2006; Parnell & De Moortel 2012). However, it has been shown that both of these mechanisms give rise to the heating in an impulsive manner (Antolin et al. 2008; Klimchuk 2015).

Impulsive events are very well observed in all layers of the solar atmosphere over a range of spatio-temporal scales (see, for example, Benz & Krucker 1998; Benz 2008). Such impulsive events are even potentially consistent with dynamics of transition region lines like Si IV (Gupta et al. 2018; Tripathi 2021; Tripathi et al. 2021), and chromospheric lines like the C II (Upendran & Tripathi 2021b) and Mg II (Upendran & Tripathi 2022). They also typically explain the dynamics and coupling in the chromosphere and transition region, with potentially explaining the formation of the solar wind (Hansteen et al. 2010), and structures like switchbacks (see Upendran & Tripathi 2022, for more details). Thus, an impulsively heated scenario may potentially explain the heating of the QS corona.

If impulsive events are to explain the temperature of the solar corona, they must follow a power-law distribution in energy of the following form: $\frac{dN}{dW} \propto W^{-\alpha}$, with $\alpha > 2$ as conjectured by Hudson (1991). However, there is a wide range of α reported in literature (see, e.g., Kuhar et al. 2018; Aschwanden 2019; Alipour et al. 2022), depending on the time, region and energy band of observation (see also, e.g., Berghmans et al. 1998; Parnell & Jupp 2000; Hannah et al. 2008; Berghmans et al. 2021).

The QS corona is generally very diffuse. The impulsive events thought to explain the QS are expected to be of the order of, or smaller than $\approx$700 km, and lie in the subpixel regime (Pauluhn & Solanki 2007). Typically, the individual events responsible for generating the QS corona may remain unresolved, and would not show a clear signature of resolved events like microflares. Hence, any statistic or model based on naive counting of occurrence of individual events in a typical QS light curve, for example, introduces a bias either toward the larger events, or an undercounting of multiple small events as one large event. These individual events, however, leave a collective imprint on the entire light curve in a statistical manner. These imprints have been shown to be statistically reflected in the intensity distribution of light curves from active regions (see, for example, the analysis by Vekstein 2009; Terzo et al. 2011; Jess et al. 2014, 2019) and coronal loops seen in X-rays (Sakamoto et al. 2009). Clearly, while individual events may not be measured, their cumulative effect on the statistical properties of intensity light curves can be leveraged to understand these events. Thus, the existence of such small-scale events may only be inferred statistically.

Typically, a "statistically-realistic" simulation would be the one which reproduces some salient properties of the observations well. A statistical and impulsively heated mechanism may leave signatures in the distribution of intensity, the characteristic temporal features, or in the thermal structure of plasma (see, e.g., Sturrock et al. 1990; Hudson 1991; Sylwester et al. 2019; Rajhans et al. 2021). Hudson (1991), for example, show that the relative interplay of frequency of occurrence of

events and the timescale of the events reflects in the temporal power spectrum of the emergent light curves. One such empirical model was proposed by Pauluhn & Solanki (2007), hereafter referred to as the `Pauluhn and Solanki Model` (PSM). PSM is an empirical model based on two key observations: the lognormal distribution of intensities in corona when taken spatially or temporally (Pauluhn et al. 2001; Andretta & Del Zanna 2014), and the power-law distribution of energies of individual events (see, e.g., Aschwanden 2019). In brief, the PSM constructs light curves through a combination of multiple impulsive events enforcing a Markovian process to generate these light curves. The amplitudes of the impulsive events are sampled from a power law, while the distribution of generated intensity is theoretically shown to be lognormal by Pauluhn & Solanki (2007). For details of PSM, see Pauluhn et al. (2001) and Pauluhn & Solanki (2007).

The PSM has been applied successfully to light curves from various regions in the solar corona (see, for example, Pauluhn & Solanki 2007; Bazarghan et al. 2008; Tajfirouze & Safari 2012; Upendran & Tripathi 2021a). In a nutshell, the application of PSM essentially involves inferring the free parameters of the model for a given light curve (or a set of light curves).

Parameter estimation may be performed using different methods. Hudson (1991) demonstrates the effect of high- and low-frequency heating on the temporal power spectrum qualitatively. However, it is desirable to actually infer the individual free parameters of the models given the light curves or power spectra, and not just obtain a qualitative match. For this purpose, we use machine learning, which is a paradigm for constraining the free parameters of a nonlinear model using data (Goodfellow et al. 2016). Upendran & Tripathi (2021a) developed an exhaustively validated machine learning inversion model for the PSM. Simply put, the inversion model employs a convolutional neural network (CNN; LeCun et al. 2015) to infer the parameters of PSM for given observed light curves as input. Upendran & Tripathi (2021a) successfully demonstrated their inversion model on a large number of light curves from Atmospheric Imaging Assembly (AIA; Lemen et al. 2012) on board the Solar Dynamics Observatory (SDO; Pesnell et al. 2012), and infer the distribution of different parameters for more than 300,000 QS light curves. This inversion scheme, which we shall henceforth call iPSM,[3] can infer the free parameters of PSM, as evidenced by the excellent match in the intensity histogram and the Mórlet wavelet power spectrum (Torrence & Compo 1998) between the simulations and observations.

The AIA data used by Upendran & Tripathi (2021a) were in units of DN s^{-1}, and did not have absolute flux calibration. Hence, while the parameters may be estimated well, it is difficult to ascertain the energy range over which these events occur. To mitigate this primary drawback, we consider the full-disk integrated, flux-calibrated data from the Solar X-ray Monitor (XSM) on board the Chandrayaan-2 mission (Vadawale et al. 2014; Shanmugam et al. 2020; Mithun et al. 2021a) of the Indian Space Research Organization. We apply the iPSM on two light curves obtained in three energy bands during the solar quiet time. Furthermore, we also generate better constraints on the bounds of PSM power-law input by applying a simple metric-based search on top of iPSM. This leads us to a better estimation of the energetics of the impulsive events in the QS.

The rest of the paper is structured as follows: in Section 2 we describe the data set used in this analysis. In Section 3 we

describe the forward model, uncertainty characterization, and the inversion scheme. In Section 4 we report the results of our inversion and various properties of our results, and finally we discuss the consequences of our results in Section 5.

2. Observations and Data

For the present work we have used the observations recorded by XSM on board the Chandrayaan-2 mission. XSM observes the Sun as a star and provides measurement of X-ray spectra in the energy range of 1–15 keV with an energy resolution of ≈175 eV at 5.9 keV and a time cadence of 1 s. It has been demonstrated that XSM has the sensitivity to carry out spectral measurements even when the solar activity is well below the A class (Mithun et al. 2020). Thus, it is possible to use XSM observations to obtain X-ray flux from the Sun during quiet phases.

We have selected XSM observations for two time periods (2019 October 17–21 and 2020 February 14–21) when there were no ARs on the solar disk as confirmed from https://solarmonitor.org. In this work, we are interested in studying the contribution of the unresolved impulsive events to the quiet coronal light curves and not the well resolved events like microflares. Thus, by visual inspection of the X-ray light curves, we removed the microflare like events studied by Vadawale et al. (2021a) so that the selected observations form a true representation of quiescent solar corona, similar to Terzo et al. (2011). This step inevitably gave rise to data gaps. However, since we are interested in a statistical study of the QS light curves, we have concatenated the light curves by ignoring the gaps and obtained a continuous time series.

For the selected duration, we generated effective area corrected and time-resolved X-ray spectra from the raw data using XSM Data Analysis Software (XSMDAS; Mithun et al. 2021b). Given the very low solar X-ray flux during these observations, the time bin size for spectra was chosen to be 2 minutes so that uncertainties on the flux due to counting statistics is typically less than 5%.

The X-ray flux light curve, $F(t)$, in the energy range E_1 to E_2 is then computed from the time-resolved spectra $S(E, t)$ as

$$F(t) = \sum_{E=E_1}^{E_2} \frac{S(E, t)\, E}{A(E)}, \tag{1}$$

where $A(E)$ is the on-axis effective area of the XSM (Vadawale et al. 2021a). For both the observations, we generated light curves using Equation (1) for the energy ranges of 1.0–1.3, 1.3–2.3, and 1.0–2.3 keV. The light curves so obtained are shown in Figure 1. Spectra above 2.3 keV are not considered as no appreciable flux is observed above that energy by XSM during QS observations.

3. Modeling

We seek to understand the properties of events that give rise to the X-ray light curves shown in Figure 1. For this purpose, we employ the PSM, which is based on the impulsive heating scenario. An impulsive event in the PSM is defined as an exponential rise of intensity to a peak value, and a subsequent exponential falloff. This is determined by the total timescale τ, which is the sum of the exponential rise (τ_r) and the decay (τ_d) timescale. These two timescales are related as $\tau_r = 0.75\tau_d$ following Pauluhn & Solanki (2007). Note that while this

---

[3] Inversion code for PSM.
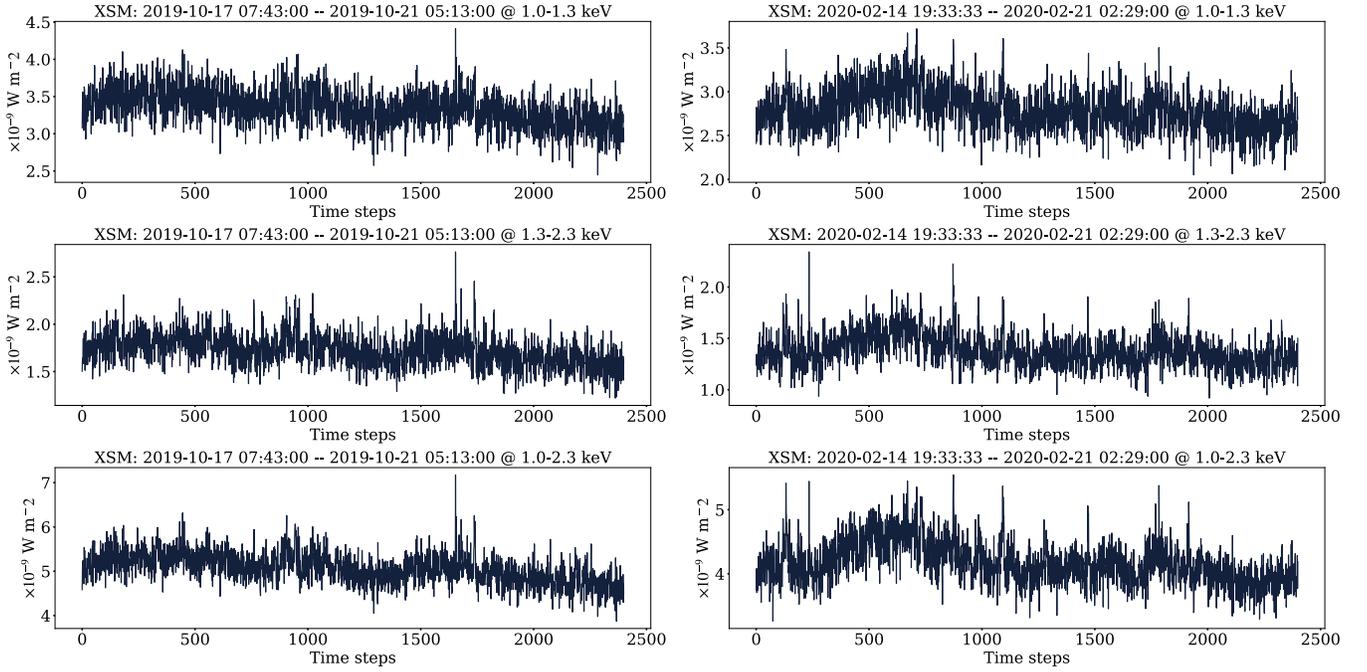
Figure 1. The XSM observed light curves considered in this work. The left (right) column is for 2019 (2020) observations. Top row is the light curve for 1.0–1.3 keV, middle row is for 1.3–2.3 keV and the bottom row is for 1.0–2.3 keV.

relation is not exact, it is observationally motivated. Zhang & Liu (2015) find a direct relation between rise and decay times, though this relation was a power law for the large flare cases considered. Also note that the constant 0.75 has been put in ad hoc by Pauluhn & Solanki (2007). The peak value, i.e., the amplitude of each event, is sampled from a power-law distribution. This power-law distribution has a slope α, with a lower and upper energy limit y_{min} and y_{max}, respectively. A multitude of impulsive events occurring at different times gives rise to the simulated light curves. The probability that an event will even occur at a time step is controlled by the flaring frequency (p_f). Hence, the PSM has five free parameters, namely, p_f, τ, α, y_{min}, and y_{max}, which fully determine a simulated light curve. This reduces our problem to the estimation of the above mentioned five parameters for XSM light curves shown in Figure 1.

The iPSM model forms the core inference block of our work. The optimization for all the five parameters is inherently difficult to perform due to degeneracy in the parameter space. Hence, iPSM performs inference of only three of the free parameters, while keeping y_{min} and y_{max} fixed. Hence, we breakdown the inversion scheme into two steps (see Figure 2), i.e., determining p_f, τ, and α in the first step and y_{max}, y_{min} in the second step by performing a fine search over the exact range of amplitude of the events.

As shown in Figure 2, each step further consists of several parts. However, the first step requires we already have a reasonable estimate of y_{max} and y_{min}. Hence, we first put reasonable bounds on the range of values y_{max} and y_{min} can take by using prior observations, and fix an initial guess. Using this y_{max} and y_{min}, we generate a bank of the PSM simulations sweeping across a range of p_f, τ, and α. We then use this simulation bank to train the iPSM (the "Training iPSM" block in Figure 2), and learn the mapping from the simulated light curves to their corresponding parameters. Finally, we perform a forward pass of the XSM light curves through the trained

model, and infer the corresponding values of p_f, τ, and α ("Inference time," pink colored section in Figure 2).

Using the inferred values of p_f, τ, and α from step 1, in step 2, we generate another bank of simulations, this time sweeping on y_{max} and y_{min}. Note that the range of y_{max} and y_{min} is within the bounds as described in step 1. Finally, by minimizing an appropriate metric, we perform a parameter sweep considering the XSM light curves to infer y_{max} and y_{min} ("Metric minimize," sea green section in Figure 2). Thus, through a two-step process, we infer all the five free parameters of the PSM.

3.1. Fixing y_{max} and y_{min}

As described above, for generating the simulation bank for iPSM in step–1, we need to fix y_{max} and y_{min}. Furthermore, we need to define bounds of y_{max} and y_{min} over which the step–2 search is performed. To do so, we first fix the upper bound of y_{max} and lower bound of y_{min} approximately, and then fix the y_{max} and y_{min} values within this range for step–1. We first define the integrated energy per flare as

$$E = 4\pi R_{1au}^2 \cdot \tau \cdot F_{median} \cdot F_{code}, \qquad (2)$$

where E is luminosity in a given energy band, F_{code} is the amplitude of an event in code units, τ is the associated timescale (in seconds), R_{1au} the distance from the Sun to Earth in meters, and F_{median} the median intensity of the XSM light curve in W m^{-2}. Note that we divide the observed light curves by their median values during training and inference time, so the event amplitudes in code units would need to be multiplied by the same scaling to get the correct dimensional values. This conversion factor in Equation (2) helps us translate from the energy of an event in code units to real units. Since we want to generate bounds on y_{max} and y_{min}, we fix the bounds for F_{code}, given other terms in Equation (2).

Equation (2) has terms on the right-hand side (except F_{code}) common for both the upper bound of y_{max} and lower bound of y_{min}. Let us consider the median intensity in the 1–2.3 keV
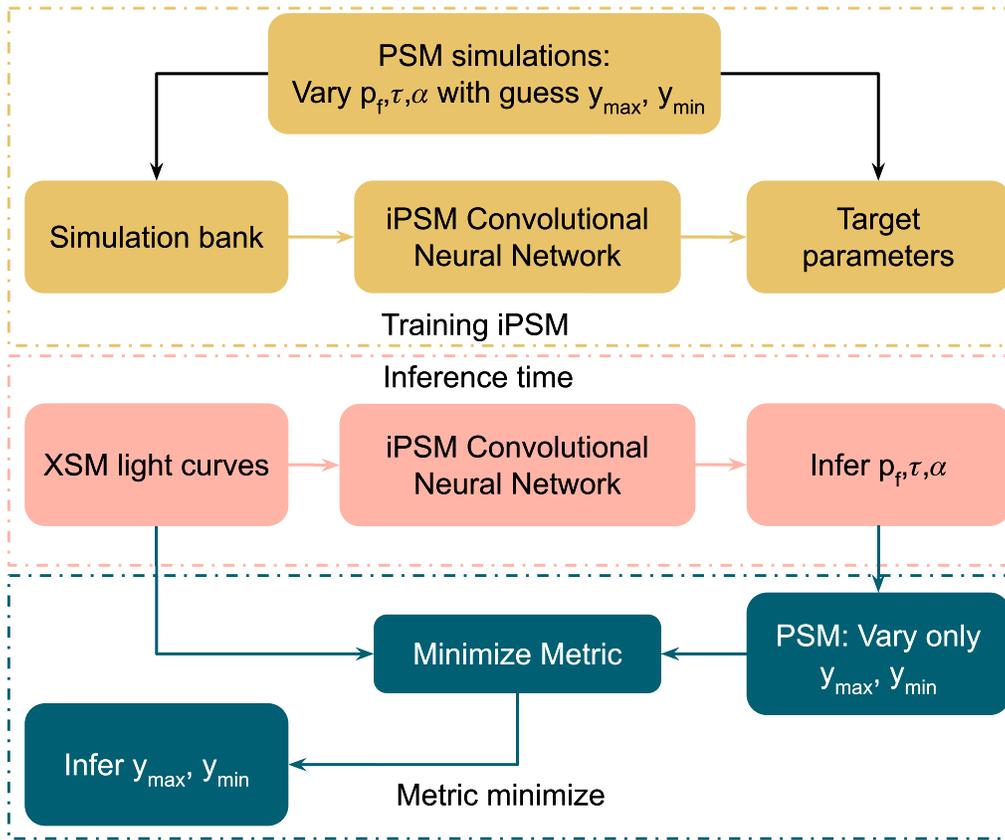
Figure 2. Flow chart detailing the various steps in our algorithm. First, the `iPSM` is trained on simulations. Next, the trained model is used to infer p_f, τ, and α. Finally, the y_{max} and y_{min} are inferred by minimizing an error metric.

energy band, which is $\approx 5 \times 10^{-9}$ W m^{-2} (see Figure 1), 1 au to be $\approx 1.5 \times 10^{14}$ m, and a maximum timescale of ≈ 720 s. We obtain this timescale from the `iPSM` inversions of light curves in the 211 Å passband of the QS, as obtained by Upendran & Tripathi (2021a). The AIA 211 Å passband corresponds to a temperature of $\log T \approx 6.2$, while the X-ray measurements typically lie in the range of $\log T \approx 6.2 - 6.8$ (Vadawale et al. 2021b). Thus, we use the 211 Å results as a proxy for the X-ray measurements here. Hence, an event with unit amplitude event (i.e $F_{\rm code} = 1$) would correspond to an energy of $\approx 10^{25}$ erg.

First, we generate an upper bound for y_{max}. We note that in our data set, all the microflares studied by Vadawale et al. (2021b) have been removed. Hence, an individual event in any of our simulation cannot be larger than the smallest flare observed by Vadawale et al. (2021b). Since we are operating in particular energy band, we redo the energy distribution computation in Vadawale et al. (2021b) for the energy band of 1–2.3 keV. The lowest energy thus inferred by Vadawale et al. (2021b) for this energy band corresponds to 10^{24} erg. This corresponds to "E" in Equation (2). Thus, $F_{\rm code}$ should be < 0.1 for the maximum amplitude condition to be satisfied. Thus, we obtain an upper bound on y_{max}—i.e., $y_{max} < 10^{-1}$.

Having fixed the upper bound for y_{max}, we turn our attention to fixing the lower bound on the y_{min}. For this, we consider the energetics of fluctuations observed in soft-X-ray light curves derived by Katsukawa & Tsuneta (2001) and Katsukawa (2003). These authors found the energies of impulsive events of $\approx 10^{20-22}$ erg to be consistent with the distribution of fluctuations of soft-X-ray light curves in active regions. Labonte & Reardon (2007), however, showed that the fluctuations in the light curves as

obtained by Katsukawa & Tsuneta (2001) are consistent with noise. Thus, we take the lower limit of the possible energies, and set a lower bound on y_{min} as 10^{20} erg, where the lower limit basically corresponds to "noise" events. This value would correspond to $y_{min} > 10^{-5}$ in code units, following Equation (2). Thus, the event amplitudes may lie only between 10^{-5} and 10^{-1}. Hence, these physical observations set the general bounds of the range of the expected energies of events.

We have now obtained the lower bound on y_{min} and the upper bound on y_{max}. To fix the values of y_{max} and y_{min} in step 1, we prototype on a very limited combination of y_{max} and y_{min}, generating one `iPSM` model for each combination. Through visual inspection, we find y_{max} and y_{min} of 5×10^{-3} and 10^{-4} (code units) to give us simulations that show a good match in the intensity distribution and wavelet power spectrum with the XSM observation. Thus, we fix y_{max} and y_{min} to be 5×10^{-3} and 10^{-4} for generating the bank of simulations for step 1 of our inversion.

3.2. Statistical Uncertainty Model

Using all the parameters discussed above, we generate simulated light curves that can be compared with the observed light curves from XSM. However, the QS is known to have weak emission in X-rays (see, for example, Brosius et al. 1997; Katsukawa & Tsuneta 2001; O'Dwyer et al. 2010), and is expected to have a nonnegligible contribution of counting statistics. Therefore, for an objective comparison, the associated simulated light curves must be incorporated with these statistical uncertainties.

For this purpose, we estimate the statistical uncertainties on the light curves by propagating the Poisson error on the observed count for each light curve. Hence, for each observed light curve to be inverted, we know the signal and the associated uncertainty at each time step.

To get a nondimensional estimate of the uncertainty as a single number for the full light curve, we first calculate the uncertainty-to-signal ratio r_t at each time step for a given XSM light curve. This provides us a measure of the "uncertainty fluctuation" as a fraction of the signal. To extract the essential features of this fluctuation while keeping the workflow simple, we consider the mode of r_t, denoted as r. This is the estimate of uncertainty as a fraction of the observed signal for the full light curve. This is justified since the variation of the mean count rates during the observations have remained nearly constant. We obtain r for each observed light curve.

To incorporate this uncertainty into each simulated light curve, we replace the intensity at each time step with a sample from a Gaussian distribution with a mean of the simulated intensity (from the PSM), and a standard deviation of r times the intensity at that time step. This is justified as while the original photon counts follow a Poisson distribution, the flux values after integration over 2 minutes are expected to follow a Gaussian distribution. Since there are six light curves, we have six associated sets of simulations for each light curve.

Finally, by taking care of all the steps explained above, we simulate the light curves. We generate simulated light curves for a duration of $2400 \times 120 = 288{,}000$ s at a time cadence of 1 s, i.e., 1 code time step = 1 s. To minimize the effect of starting seed, we generate the simulations with extra 1600 s, and throw away the first and last 800 s. The simulations are then rebinned at 120 s cadence, giving rise to 2400 time points to match the observations.

We incorporate the statistical uncertainties to each simulated light curve, and normalize each by it is median value as a preprocessing step to the iPSM. After parameter inference, we construct the best-matching simulations by multiplying the median normalized simulations with the median value of the corresponding observation. This gives us simulation light curves in the units of W m^{-2}. Since we are scaling the intensities in the simulations, we also scale the corresponding y_{max} and y_{min} values, which determine the amplitude of these events, in the same way.

For step 1, we generate the bank of simulations by varying p_f between 3 and 57 events per minute, , which translates to p_f between 0.05 and 0.95 events per second in steps of 0.01 events per second. . The timescale τ is varied between 1 and 500 s in steps of 10 s, while α is varied between 1.5 and 3.0 in steps of 0.1. This parameter space is similar to Upendran & Tripathi (2021a). We have, however, reduced the maximum value of τ (in seconds), since we expect X-ray observations to show much shorter timescales than EUV observations, as seen by Upendran & Tripathi (2021a). With the step 1 simulation bank ready, we are ready to perform step 1 inference of PSM parameters.

3.3. Inversion Scheme: The iPSM

The iPSM is a deep-learning model as defined in Upendran & Tripathi (2021a). This is a 1D CNN model that takes in the light curves, and maps them to their corresponding free parameter set—p_f, τ, and α. We describe the network architecture briefly below, while the details are exactly as described in Upendran & Tripathi (2021a). In essence, iPSM contains multiple convolution layers sandwiched with non-linear transformations called activation functions. This forms the basic "learning ability" of the iPSM.

During training time, a cost function is minimized to train the trainable parameters (weights) of the network. The hyperparameters, which must be fixed by hand, are the same as those used in Upendran & Tripathi (2021a). However, note that since the simulations in this work need to be uncertainty-incorporated, we retrain the model from scratch for the new set of simulated light curves. We generate six inversion models in total corresponding to each light curve.

The iPSM also generates epistemic uncertainties associated with every inversion. This is accomplished by randomly switching off certain neurons during inference time (Hinton et al. 2012), and performing a Monte Carlo forward pass. The obtained uncertainty is a reflection of how much weight parameter space has not been explored by the iPSM (Gal 2016).

The simulated light curves for each model are split into training set (80%) and testing set (20%). The model is trained on the training set, while the evaluation on the testing set is used to mark the convergence of the model. Following Upendran & Tripathi (2021a), we use the coefficient of determination (R^2) as a measure of goodness of fit of the model. Simply put, R^2 performs a pointwise comparison between two arrays. If the two arrays are perfectly correlated, $R^2 = 1$. The worse the correlation, the lower R^2 is. We compare the actual simulation parameters with those obtained by inversion from the iPSM. All of our models show $R^2 > 0.98$ for p_f and τ, while the R^2 for α are more than 0.91. This step is depicted graphically as the yellow and pink flow diagrams in Figure 2. Thus, we infer p_f, τ, and α for each XSM light curve from step 1.

3.4. Inversion Scheme: Metric Minimization

In step 1, we have inferred three parameters p_f, τ, and α for fixed values of y_{min} and y_{max}. In step 2, we fix these three parameters and generate a new set of light curves by sweeping y_{max} and y_{min}. We sweep y_{max} between 9×10^{-4} and 5×10^{-2} with 45 steps in $\log_{10}$, and y_{min} between 1×10^{-5} and 5×10^{-4} for 36 steps in $\log_{10}$. On these light curves we incorporate the photon counting uncertainties as described in Section 3.2. These light curves serve as a bank from which we may perform an inexpensive, simple search to generate better constraints on y_{min} and y_{max}. However, to do so, we need to define a metric that we may then minimize. Since our qualitative "best fit" is determined by a good match between the simulation and observation in terms of intensity distribution and power spectrum, we define a simple metric in Equation (3) as

$$m = \max((\mathrm{CDF}_O - \mathrm{CDF}_S)^2) + \max(((P_O - P_S)/P_O)^2). \quad (3)$$

Here the subscripts O and S correspond to observation and simulation respectively. The first term finds the maximum of absolute difference between the cumulative distribution function of the two light curves. The second term finds the maximum relative wavelet power mismatch between the two light curves.

With this metric, we then perform a grid search, and find the combination that gives us the lowest possible metric value. The corresponding y_{max} and y_{min} are then taken up as the "inferred" final values.
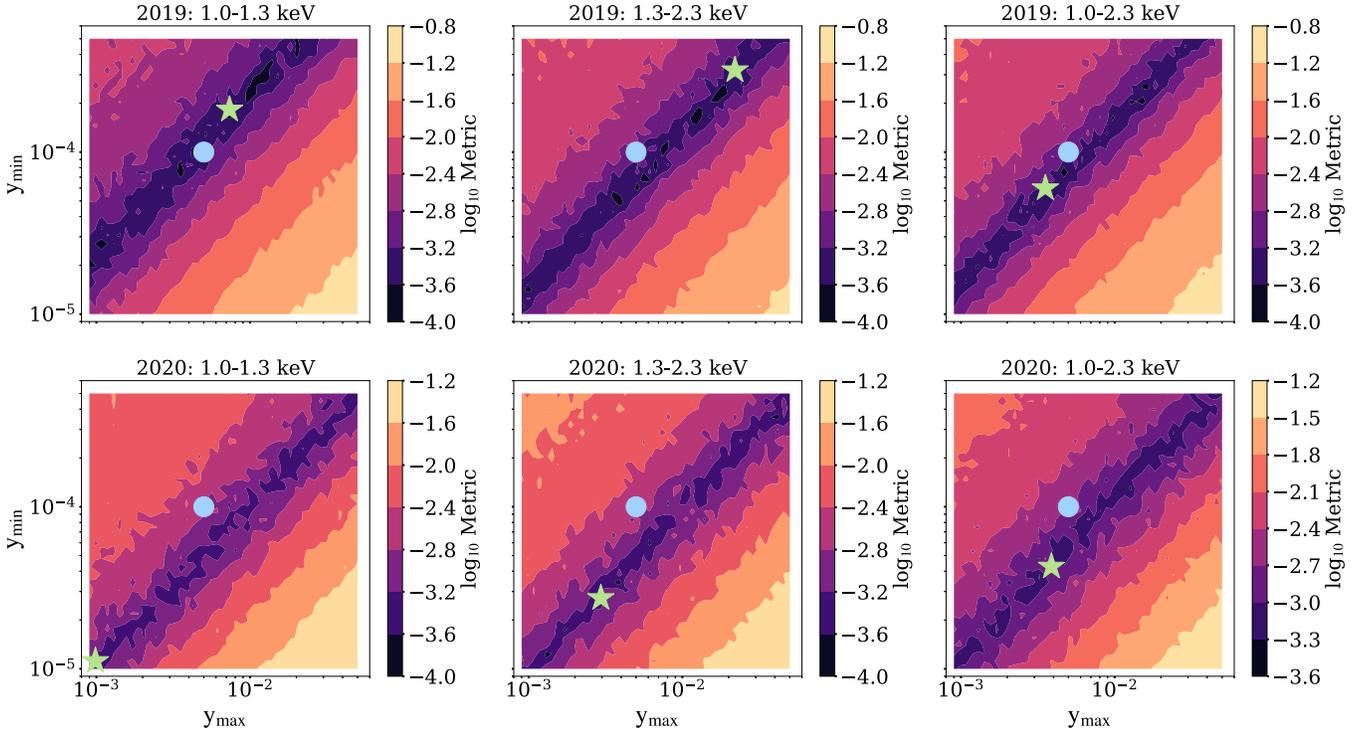
Figure 3. The variation of metric with y_{max} (x-axis) and y_{min}(y-axis). The two parameters are presented here in code units (note the log scale), while the metric is presented in scale of $\log_{10}$. The blue circle shows the originally selected y_{max} and y_{min} (as used by the iPSM), while the green star corresponds to be combination with lowest metric value.

4. Analysis and Results

4.1. Light-curve Inversions

Applying our two-step procedure described in Section 3, we obtain the "best-fit" parameters of the PSM simulations. In Figure 3, we present the metric surface from step–2 as a function of the swept range of y_{max} and y_{min}, where the metric value is lower for darker color. Note that we have displayed the metric in log scale. The blue circle represents the originally prefixed y_{max} and y_{min} for step–1, while the green star is the y_{max} and y_{min} solution inferred from step–2 parameter search.

Figure 3 reveals a number of salient features about our inferred solution(s). First, there is a whole diagonal of "good" solutions, showcasing the degeneracy between y_{max} and y_{min}. Second, the prefixed y_{max} and y_{min} lie very close the diagonal ridge of good solutions, thereby also justifying our choice of initial guess for y_{max} and y_{min}. Third, the final good solutions are sometimes quite close to the prefixed values, while sometimes they change by 1 order of magnitude. The final amplitudes, however, would depend on the median flux value. Therefore, the constraint is strongly performed for the ratio of y_{max} and y_{min}. On the whole, a very strong global minimum is not clearly seen for constraining y_{max} and y_{min}. However, the solutions as we shall see next give rise to a very good representations of the observed light curves.

We now present the inversion results for the two light curves obtained by integrating the signal between 1 and 2.3 keV energy band in Figure 4. The results for other light curves are presented in Appendix A1.

In Figure 4, we show the light curves (panel (a)), intensity distributions (panel (b)), wavelet power spectrum (panel (c)), and cumulative distribution function (CDF; panel (d)). The orange represents the observation and the black represents the

PSM forward model of the best-fit parameters. Note that simulated light curve is uncertainty-incorporated. The uncertainty bands in the power spectrum correspond to 1σ standard deviation in time. The top four panels are for data recorded in 2019 and the bottom four are for those in 2020. Note again that a statistically accurate simulation must capture the intensity distribution well. Similarly, such a simulation must also capture the essential frequencies in the time series which have excess power. These are represented by the histogram (and CDF) and the wavelet power spectrum. The presence of peaks at similar frequencies in the power spectrum gives us the scales of importance, though we emphasize that the exact amount of power need not exactly match. The plots reveal a good correspondence between the observed and simulated light curve, both in matching the distribution, and wavelet power at different scales. Thus, the two-step inversion scheme with iPSM successfully in captures the necessary information from the presented observations.

We summarize the inversion parameters for all the six light curves in Table. 1. We note that the flaring frequency p_f ranges from 24 to 35 events per minute and the timescale τ ranges from $\approx$6 to 12 minutes with maximum uncertainty of the order of a minute. For all the light curves, the inversion gives us power-law slopes of $\leqslant$2.0. Finally, y_{max} generally ranges from 7×10^{-11}–1.26×10^{-10} W m^{-2}, while y_{min} ranges from 6×10^{-13}–2×10^{-12} W m^{-2}.

4.2. Energetics

We now have a train of events giving rise to each of the observed light curves. Our goal is to study the energetics of these events. For this purpose, we first convert the obtained intensities into fluxes and energies following Equation (2). Since we would be integrating only in a particular energy band, they would

XSM: 2019-10-17 07:43:00 -- 2019-10-21 05:13:00 @ 1.0-2.3 keV

α = 1.87±0.15 , y_{min} = 2.12e-12 W m^{-2} p_f = 28.00±2.16 min^{-1}, y_{max} = 1.26e-10 W m^{-2} τ = 11.80±1.05 min,
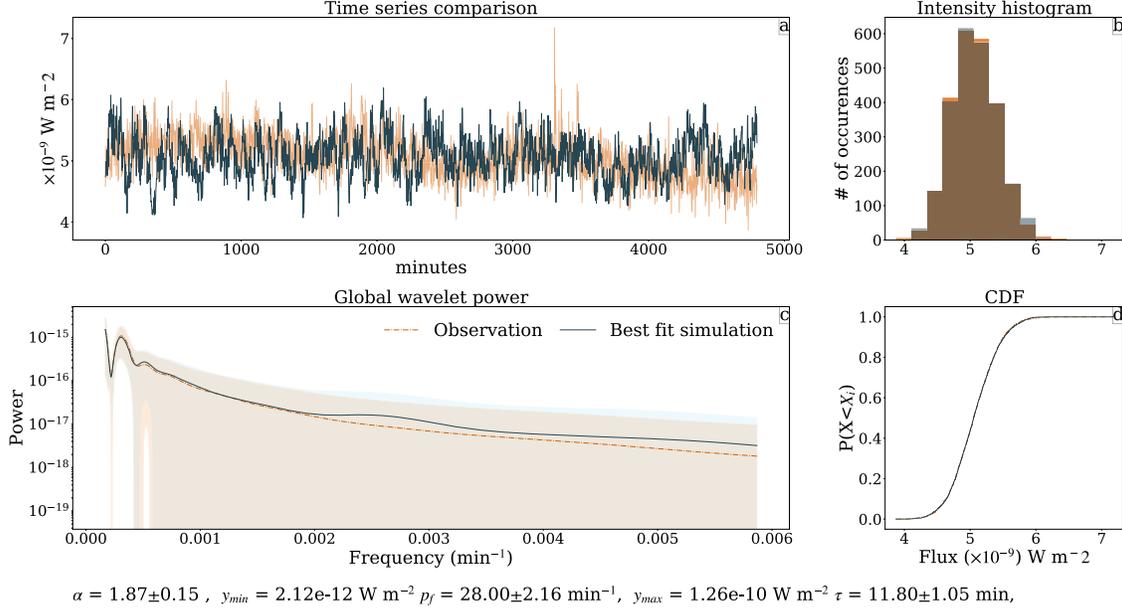
I. 1-2.3 keV from October 2019

XSM: 2020-02-14 19:33:33 -- 2020-02-21 02:29:00 @ 1.0-2.3 keV

α = 1.58±0.12 , y_{min} = 1.00e-12 W m^{-2} p_f = 34.17±1.97 min^{-1}, y_{max} = 9.07e-11 W m^{-2} τ = 8.26±0.67 min,
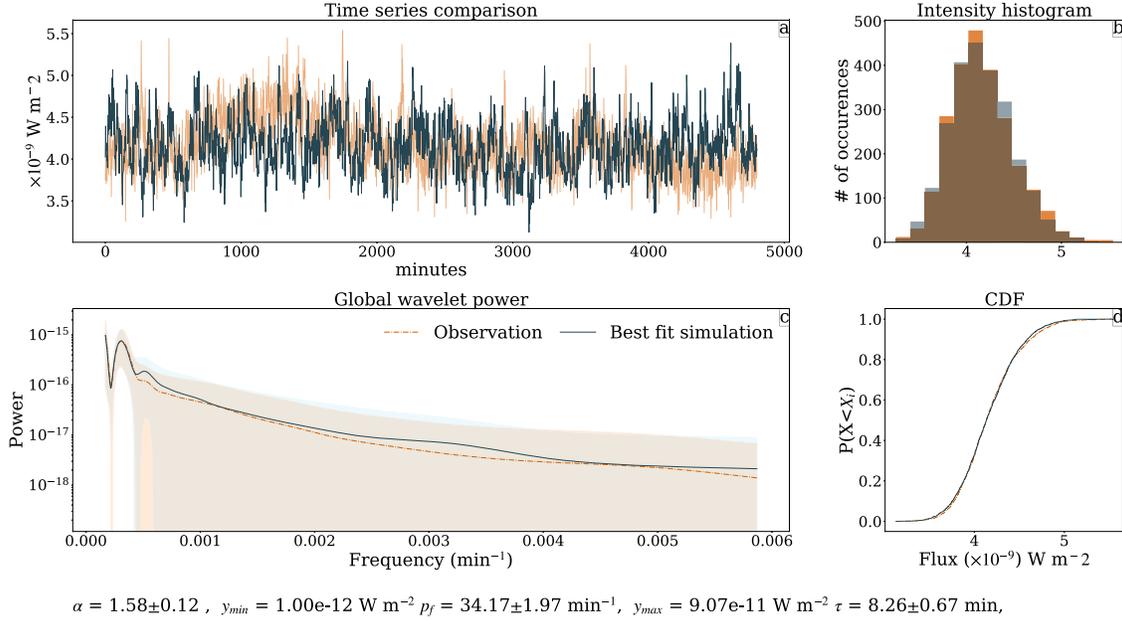
II. 1-2.3 keV from February 2020

Figure 4. Comparison of the observed light curve from XSM (orange), and the `PSM` forward model of best-fit parameters inferred from our inversion code (black) in 1–2.3 keV energy band from 2019 (subfigure: I) and 2020 (subfigure: II). Each subfigure has four panels depicting the following. Panel (a): observed and simulated light curves. Panel (b): distribution of observed and simulated light-curve intensities. Panel (c): global Morlét power for observation and simulations, with the uncertainties presented in orange and blue bands. Panel (d): comparison of simulation and observation intensity CDF. The inset reports the inferred parameter set for the respective data.

correspond to a "lower bound" of energy. The energy estimates are better representatives of the energy content of these events if larger energy bands are considered. Hence we consider the energies in the widest 1–2.3 keV passband. We find that our energies typically range between 10^{21} and 2×10^{23} erg for this passband, with α shallower than 2.0. These events will thus correspond to the nanoflare or even picoflare energy range.

To understand the average radiative loss flux, we define the average amplitude of flare in a given time series (A) following Pauluhn & Solanki ([2007]) as

$$A := \left(\frac{1 - \alpha}{2 - \alpha} \right) \cdot \left(\frac{y_{\max}^{2-\alpha} - y_{\min}^{2-\alpha}}{y_{\max}^{1-\alpha} - y_{\min}^{1-\alpha}} \right). \quad (4)$$

Table 1
Summary of the Inferred Parameters for the Six Light Curves

Parameter	1.0–1.3 keV		1.0–2.3 keV		1.3–2.3 keV	
	2019	2020	2019	2020	2019	2020
p_f (events minute^{-1})	27.89 ± 1.67	33.18 ± 1.87	28.00 ± 2.16	34.17 ± 1.97	25.42 ± 1.57	24.95 ± 5.15
τ (minutes)	10.56 ± 0.88	9.12 ± 0.73	11.80 ± 1.05	8.26 ± 0.67	9.29 ± 0.79	6.56 ± 0.56
α	2.00 ± 0.12	1.74 ± 0.15	1.87 ± 0.15	1.58 ± 0.12	1.94 ± 0.13	1.56 ± 0.13
y_{max} (W m^{-2})	8.14×10^{-11}	7.30×10^{-11}	1.26×10^{-10}	9.07×10^{-11}	7.71×10^{-11}	6.86×10^{-11}
y_{min} (W m^{-2})	2.03×10^{-12}	8.28×10^{-13}	2.12×10^{-12}	1.00×10^{-12}	1.12×10^{-12}	6.36×10^{-13}

Table 2
Radiative Losses in erg cm^{-2} s^{-1} for the Three Energy Passbands and Two Years

Energy Band (keV)	2019	2020
1.0–1.3	$4.18 \pm 0.65 \times 10^3$	$3.02 \pm 0.74 \times 10^3$
1.0–2.3	$6.29 \pm 1.37 \times 10^3$	$4.39 \pm 0.92 \times 10^3$
1.3–2.3	$2.26 \pm 0.43 \times 10^3$	$1.82 \pm 0.57 \times 10^3$

The amplitude of the flare as defined in Equation (4) is in code units, which can be converted into real units of energies following Equation (2). Inherently, we assume that the corresponding energy obtained is emitted isotropically by the Sun. To estimate the amount of energy emitted across the whole time series, we also need the frequency of occurrence of these events (p_f). Hence, for a given flaring frequency of p_f (events per second), the amount of energy radiated per unit time would be $p_f \cdot E$. Thus, the radiative flux loss from unit solar area (since we are performing full-disk integration) would be

$$\mathrm{RL} := \frac{p_f \, 4\pi R_{1au}^2 \cdot \tau}{A_{\odot,\mathrm{disk}}} A. \qquad (5)$$

We find the radiative flux losses to be $\approx 5 \times 10^3$ erg cm^{-2} s^{-1} in the 1–2.3 keV energy band, while they are $\approx 3.5 \times 10^3$ and $\approx 2 \times 10^3$ erg cm^{-2} s^{-1} in the 1–1.3 and 1.3–2.3 keV energy bands, with error bars on each term. While the full set of results are presented in the Appendix and in Table 2, the losses are typically of the order of 10^3 erg cm^{-2} s^{-1}.

5. Discussion

In this paper we study the QS heating and its energetics using XSM observations. To this end we use the empirical impulsive heating scheme of PSM as the ground truth. We have deployed a two-step inversion scheme using the machine-learning iPSM coupled to a metric-based parameter search to infer the PSM parameters of our QS light curves. This inversion scheme let us infer the flaring frequency (p_f), the timescale (τ), and the power-law slope (α), as well as the bounds of the power law (y_{max}, y_{min}) for any given light curve. By incorporating uncertainty model for the observed light curves, we perform the inference on full-disk integrated X-ray observations. The obtained results are summarized in Table 1.

We find that the flaring frequency is ≈ 24–35 events per minute. . This flaring frequency is $10 \times$ larger than those reported by Upendran & Tripathi (2021a) based on AIA observations, who found $p_f \approx 2.5$ events per minute. . These two results may be reconciled by noting that the average flaring amplitude (A) defined in Equation (4) is $\approx 10^{-3}$ in this study, while Upendran & Tripathi (2021a) find $A \approx 10^{-2}$ in EUV.

This shows that an approximately $10 \times$ reduction in the flare amplitude has resulted in an approximately $10 \times$ increase in flaring frequency (p_f). This is consistent with the finding of Upendran & Tripathi (2021a) that p_f is found to reduce with increasing event amplitude. Thus, results for flaring frequency (p_f) obtained here for X-ray observations is consistent with their EUV counterparts shown in Upendran & Tripathi (2021a), and strongly indicate the presence of an energy reservoir that may be depleted by large events occurring infrequently, or small events occurring more frequently. This flaring frequency translates to ≈ 300 events in a full-disk quiet coronal image in the 1–2.3 keV energy range, if an integration over ≈ 11 minutes is performed. However, note that we have selected extremely quiet times in this analysis, where there are no visible flares. Thus, the whole solar corona need not be at temperatures emitting strongly in the 1–2.3 keV energy range of X-rays. Furthermore, these events would have a typical amplitude of 10^{-13}–10^{-11} W m^{-2}. This implies that even for regions emitting most strongly in X-rays in these quiet times, the events may not be detectable discretely upon incorporation of noise and statistical uncertainties. Thus, we expect only as a diffuse background to be seen with current instrumentation.

We further find that the event timescale ranges from ≈ 6–11 minutes. Based on EUV observations from AIA, Upendran & Tripathi (2021a) showed that the event timescales reduce with increasing temperature, i.e., from ≈ 16 minutes in 171 Å ($\log T \approx 5.85$) to ≈ 12 minutes in 211 Å ($\log T \approx 6.2$). Since the observations reported here are at higher temperature, the obtained results are consistent with those from EUV. However, note that these are only the mean values of a distribution of timescales as inferred by Upendran & Tripathi (2021a).

We may also compare the properties of these unresolved events with those of resolved microflares. Sylwester et al. (2019), for example, studied microflares in the 1.2–15 keV energy range using data from SphinX (Sylwester et al. 2008), with similar events studied by Vadawale et al. (2021a). They find the median temperatures of $\log T \approx 6.3$, while the timescales range from $\leqslant 1$ to ≈ 10 minutes. Thus, the timescales we obtain are typically of the order of, or even slightly longer than, those obtained by Sylwester et al. (2019)—though we emphasize that timescales are consistent within the uncertainties.

Finally, we obtain α between 2.0 and 1.56 in this study, which are far flatter than those obtained by Upendran & Tripathi (2021a), who find $\alpha \geqslant 2$. However, note that the median α in Upendran & Tripathi (2021a) varies from 2.26 in 171 Å to 2.07 in the 211 Å passband. Consistent with this trend, we also find the α from X-rays to be smaller. Moreover, from Table 1, we see that the α value reduces with increasing energy (from 1–1.3 to 1.3–2.3 keV). However, we note that the increase is only in the mean value, but within the error bars they are consistent. On the whole, there appears to be a

particular flattening of α with the increasing temperature of plasma. Thus, our results are consistent with those of Upendran & Tripathi (2021a) based on AIA observations.

We emphasize, however, that the smaller α for higher temperatures is intriguing, i.e., for a given range of amplitudes, a larger α would have infrequent outlier intensities. However, a smaller α, as inferred here, implies that these outlier events start to become the norm, implying that the typical amplitude of events is nearly constant. Moreover, Vadawale et al. (2021b) find the power-law slope to agree with 2 for the microflare observations using the same instrument and for the same time periods. This raises the question of a possible change of the underlying mechanism of heating from higher energies to lower energies, which reflects as differences in the power-law exponent.

We note that the obtained energy of the impulsive events are typically in the nanoflare/picoflare regime and vary in the range of 10^{21}–2×10^{23} erg. These values are typically of the scale of thermal energy as measured by Sylwester et al. (2010) for typical solar quiet times, though we note that we report only a conversion of luminosity to energy, and not the thermal energy itself. Considering a very small range of energies the actual value of α may not even have a strong meaning. It may simply suggest that the events of $\approx 10^{23}$ erg are dominant over events with energy $\approx 10^{21}$ erg. Therefore, it is imperative to not consider just the parameter α, but also consider the radiative flux in the events to get a better estimate.

Due to the flux-calibrated data of XSM, we can estimate the radiative energy loss from the quiet corona. We find the flux to be $\approx 10^3 \, \mathrm{erg \, cm^{-2} \, s^{-1}}$ for the full energy range of 1–2.3 keV. This flux is 2 orders of magnitude lower than the radiative loss estimates in the quiet corona by Withbroe & Noyes (1977). Prima facie, it suggests that such subpixel impulsive events may not have enough energy to maintain the quiet corona. However, we must note that the energy estimate presented here only provides a lower bound, since the energy is radiated away in many wavelengths. A better way would be to estimate the "thermal energy" content of the impulsive events, which is not possible in our case due to lack of spatial content, i.e., a length measure along the line of sight.

A caveat exists in the estimation of only the radiative energy in the given passbands of XSM. Similar to Upendran & Tripathi (2021a), it is possible that some events may generate a response only in particular energy bands. Hence, the energetics of these events must be estimated by considering multiple energy bands in tandem while also introducing spectroscopic filling factors. This is a possible trajectory for the improvement of the PSM in the future.

Appendix

## A1. Light-curve Comparison for Other Energy Bands

In this section, we present the light-curve comparison for all the energy bands. The presentation follows same convention as Figure 4. These are presented as Figure 5 and Figure 6.

A2. Distribution of Events and Their Energetics

In Figure 7, we compare the distribution of the events from this work with those measured by Vadawale et al. (2021b), while in Table 2, we report the radiative losses in all the energy bands for both the years. The error bars are obtained by propagating the Monte Carlo uncertainties in the inverted parameters across the different equations.

Since we have an exact functional form for the event distribution, we sample 10 points between $y_{\min}$ and $y_{\max}$, and plot our results for the 1–2.3 keV passband in Figure 7. The pink color shows the data for 2019 and cyan color is for 2020, while the black color corresponds to the data by Vadawale et al. (2021b). The overplotted dotted–dashed back line represents a power law with $\alpha = 2.0$.

XSM: 2019-10-17 07:43:00 -- 2019-10-21 05:13:00 @ 1.0-1.3 keV

$\alpha = 2.00\pm0.12$, $y_{min} = 2.03\text{e-}12$ W m^{-2} $p_f = 27.89\pm1.67$ min^{-1}, $y_{max} = 8.14\text{e-}11$ W m^{-2} $\tau = 10.56\pm0.88$ min,

XSM: 2020-02-14 19:33:33 -- 2020-02-21 02:29:00 @ 1.0-1.3 keV

$\alpha = 1.74\pm0.15$, $y_{min} = 8.28\text{e-}13$ W m^{-2} $p_f = 33.18\pm1.87$ min^{-1}, $y_{max} = 7.30\text{e-}11$ W m^{-2} $\tau = 9.12\pm0.73$ min,
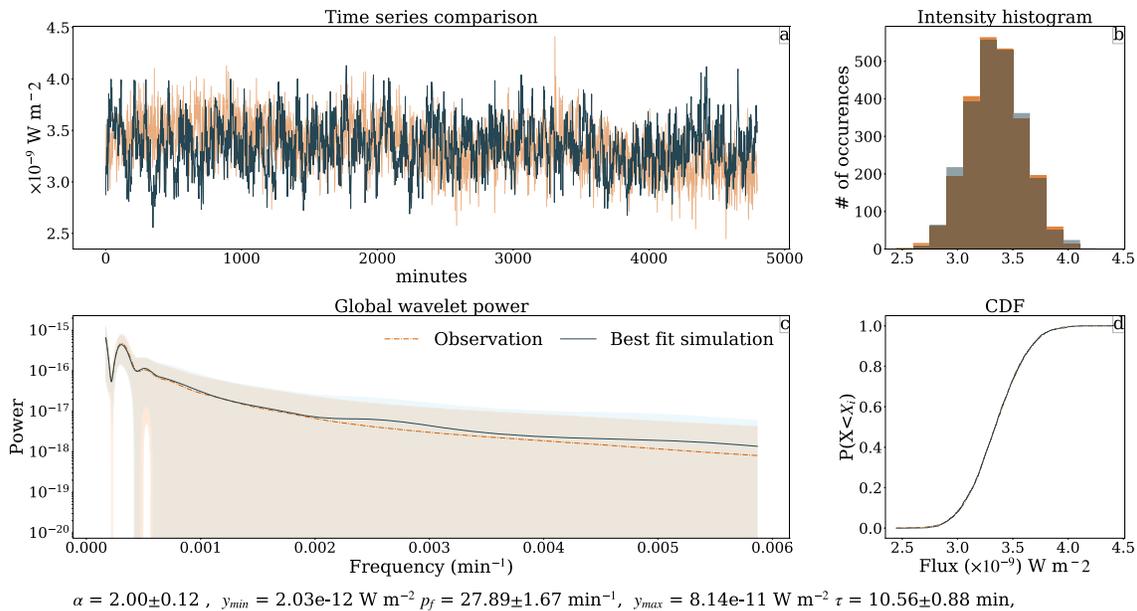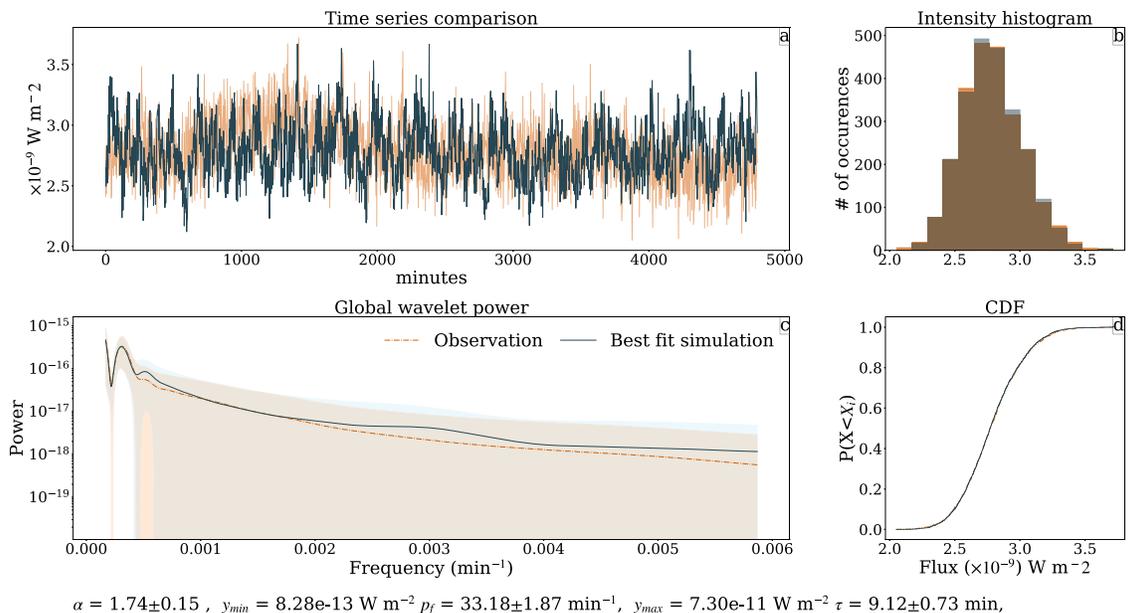
Figure 5. Same as Figure 4, but for 1.3–2.3 keV band.

XSM: 2019-10-17 07:43:00 -- 2019-10-21 05:13:00 @ 1.3-2.3 keV
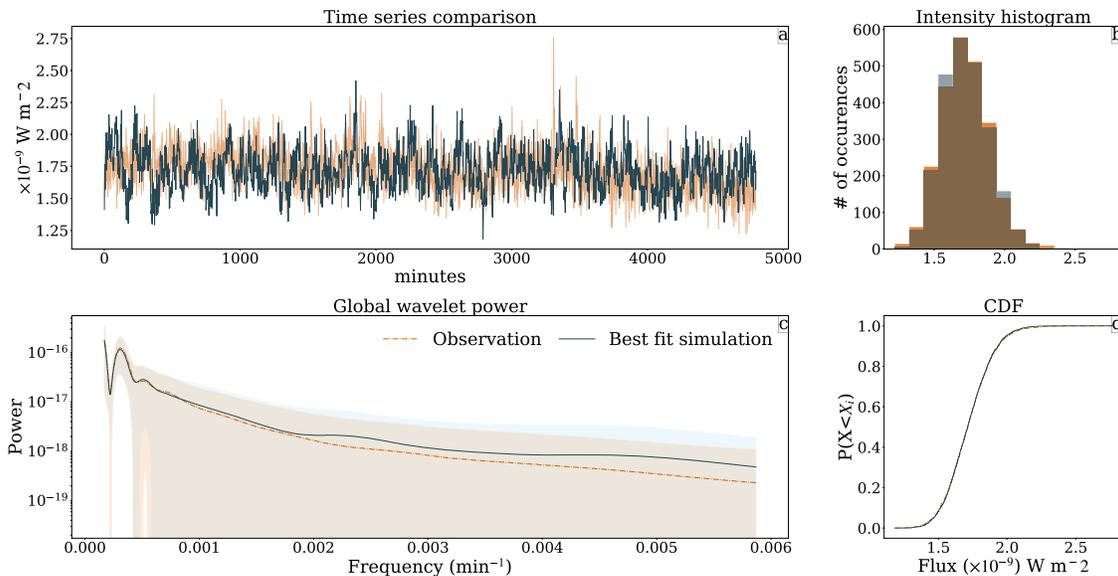
$\alpha = 1.94\pm0.13$, $y_{min} = 1.12\text{e-}12$ W m^{-2} $p_f = 25.42\pm1.57$ min^{-1}, $y_{max} = 7.71\text{e-}11$ W m^{-2} $\tau = 9.29\pm0.79$ min,

XSM: 2020-02-14 19:33:33 -- 2020-02-21 02:29:00 @ 1.3-2.3 keV
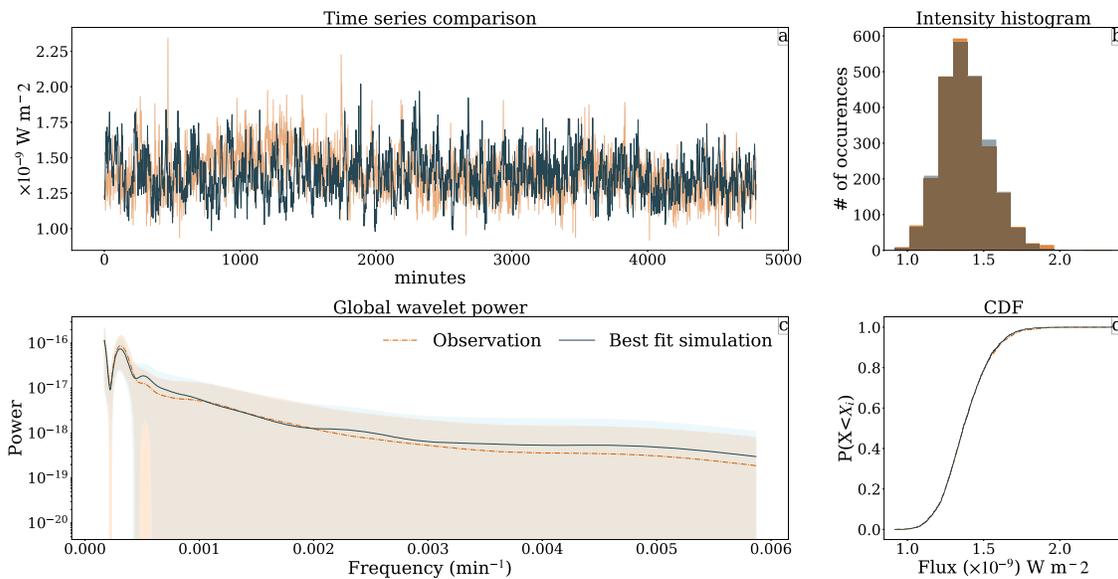
$\alpha = 1.56\pm0.13$, $y_{min} = 6.36\text{e-}13$ W m^{-2} $p_f = 24.95\pm5.15$ min^{-1}, $y_{max} = 6.86\text{e-}11$ W m^{-2} $\tau = 6.56\pm0.56$ min,

Figure 6. Same as Figure 4, but for 1.3–2.3 keV band for the segment from year 2020.
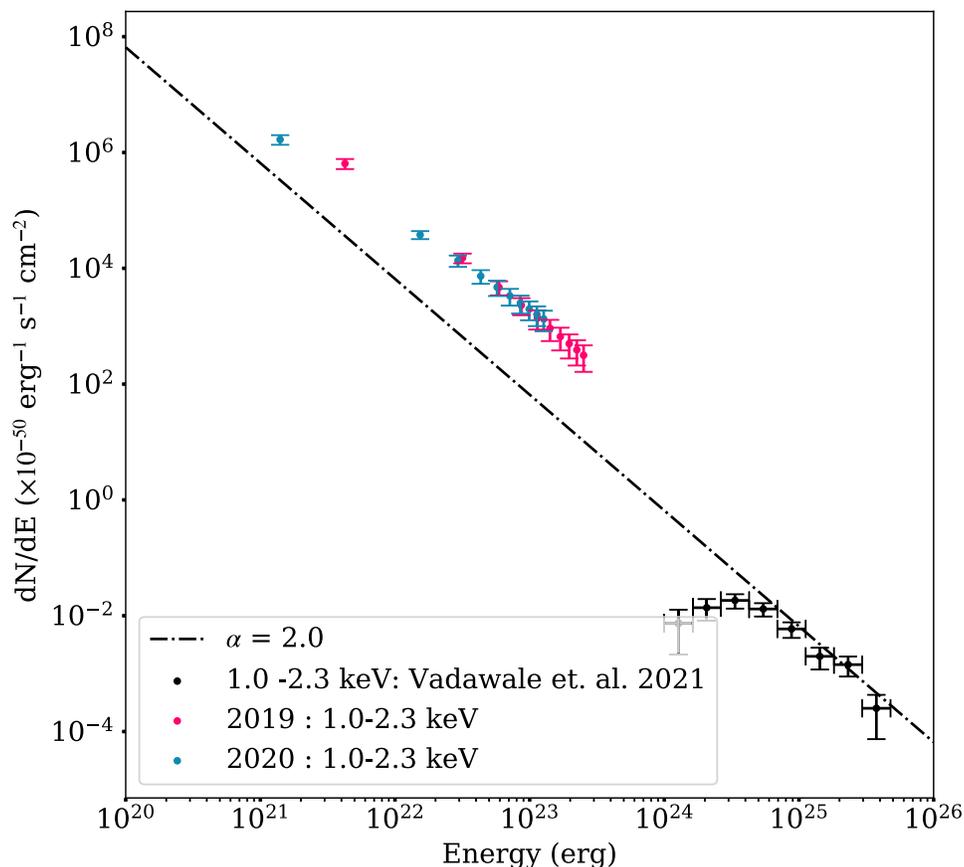
Figure 7. Frequency distribution of impulsive events inferred from the observations in year 2019 (pink) and 2020 (cyan). The scatter is frequency distribution of event energies from the model. The error bars on inferred parameters are obtained by propagating the Monte Carlo uncertainties. The black scatter shows the inferred frequency distribution from Vadawale et al. (2021b), while the black dotted–dashed line corresponds to $\alpha = 2.0$.

ORCID iDs

Vishal Upendran ⬤ https://orcid.org/0000-0002-9253-6093
Durgesh Tripathi ⬤ https://orcid.org/0000-0003-1689-6254
N. P. S. Mithun ⬤ https://orcid.org/0000-0003-3431-6110
Santosh Vadawale ⬤ https://orcid.org/0000-0002-2050-0913
Anil Bhardwaj ⬤ https://orcid.org/0000-0003-1693-453X

References

Abadi, M., Barham, P., Chen, J., et al. 2016, arXiv:1605.08695
Alfvén, H., & Lindblad, B. 1947, MNRAS, 107, 211
Alipour, N., Safari, H., Verbeeck, C., et al. 2022, A&A, 663, A128
Andretta, V., & Del Zanna, G. 2014, A&A, 563, A26
Antolin, P., Shibata, K., Kudoh, T., Shiota, D., & Brooks, D. 2008, ApJ, 688, 669
Aschwanden, M. J. 2019, New Millennium Solar Physics, Astrophysics and Space Science Libary, Vol. 458 (Cham: Springer)
Bazarghan, M., Safari, H., Innes, D. E., Karami, E., & Solanki, S. K. 2008, A&A, 492, L13
Behnel, S., Bradshaw, R., Citro, C., et al. 2011, CSE, 13, 31
Benz, A. O. 2008, LRSP, 5, 1
Benz, A. O., & Krucker, S. 1998, SoPh, 182, 349
Berghmans, D., Auchère, F., Long, D., et al. 2021, A&A, 656, L4
Berghmans, D., Clette, F., & Moses, D. 1998, A&A, 336, 1039
Brosius, J. W., Davila, J. M., Thomas, R. J., et al. 1997, ApJ, 477, 969
Chiueh, T., & Zweibel, E. G. 1987, ApJ, 317, 900
Gal, Y. 2016, PhD thesis, Univ. Cambridge
Goodfellow, I., Bengio, Y., & Courville, A. 2016, Deep Learning (Cambridge, MA: MIT Press), http://www.deeplearningbook.org
Gupta, G. R., Sarkar, A., & Tripathi, D. 2018, ApJ, 857, 137
Hannah, I. G., Christe, S., Krucker, S., et al. 2008, ApJ, 677, 704

Hansteen, V. H., Hara, H., De Pontieu, B., & Carlsson, M. 2010, ApJ, 718, 1070
Harris, C. R., Millman, K. J., van der Walt, S. J., et al. 2020, Natur, 585, 357
Hinton, G. E., Srivastava, N., Krizhevsky, A., Sutskever, I., & Salakhutdinov, R. R. 2012, arXiv:1207.0580
Hudson, H. S. 1991, SoPh, 133, 357
Hunter, J. D. 2007, CSE, 9, 90
Jess, D. B., Dillon, C. J., Kirk, M. S., et al. 2019, ApJ, 871, 133
Jess, D. B., Mathioudakis, M., & Keys, P. H. 2014, ApJ, 795, 172
Katsukawa, Y. 2003, PASJ, 55, 1025
Katsukawa, Y., & Tsuneta, S. 2001, ApJ, 557, 343
Klimchuk, J. A. 2006, SoPh, 234, 41
Klimchuk, J. A. 2015, RSPTA, 373, 20140256
Kluyver, T., Ragan-Kelley, B., Pérez, F., et al. 2016, in Positioning and Power in Academic Publishing: Players, Agents and Agendas, ed. F. Loizides & B. Schmidt (Amsterdam: IOS Press), 87
Kuhar, M., Krucker, S., Glesener, L., et al. 2018, ApJL, 856, L32
Labonte, B. J., & Reardon, K. P. 2007, SoPh, 240, 387
LeCun, Y., Bengio, Y., & Hinton, G. 2015, Natur, 521, 436
Lemen, J. R., Title, A. M., Akin, D. J., et al. 2012, SoPh, 275, 17
McKerns, M. M., Strand, L., Sullivan, T., Fang, A., & Aivazis, M. A. 2012, arXiv:1202.1056
Mithun, N. P. S., Vadawale, S. V., Sarkar, A., et al. 2020, SoPh, 295, 139
Mithun, N. P. S., Vadawale, S. V., Shanmugam, M., et al. 2021a, ExA, 51, 33
Mithun, N. P. S., Vadawale, S. V., Patel, A. R., et al. 2021b, A&C, 34, 100449
O'Dwyer, B., Del Zanna, G., Mason, H. E., Weber, M. A., & Tripathi, D. 2010, A&A, 521, A21
Osterbrock, D. E. 1961, ApJ, 134, 347
Parker, E. N. 1972, ApJ, 174, 499
Parker, E. N. 1988, ApJ, 330, 474
Parnell, C. E., & De Moortel, I. 2012, RSPTA, 370, 3217
Parnell, C. E., & Jupp, P. E. 2000, ApJ, 529, 554
Pauluhn, A., & Solanki, S. K. 2007, A&A, 462, 311
Pauluhn, A., Solanki, S. K., Rüedi, I., Landi, E., & Schühle, U. 2001, in IAU Symp. 203, Recent Insights into the Physics of the Sun and Heliosphere:

Highlights from SOHO and Other Space Missions, ed. P. Brekke, B. Fleck, & J. B. Gurman (San Francisco, CA: ASP), 416

Pesnell, W. D., Thompson, B. J., & Chamberlin, P. C. 2012, SoPh, 275, 3

Rajhans, A., Tripathi, D., & Kashyap, V. L. 2021, ApJ, 917, 29

Sakamoto, Y., Tsuneta, S., & Vekstein, G. 2009, ApJ, 703, 2118

Shanmugam, M., Vadawale, S. V., Patel, A. R., et al. 2020, CSci, 118, 45

Sturrock, P. A., Dixon, W. W., Klimchuk, J. A., & Antiochos, S. K. 1990, ApJL, 356, L31

Sylwester, B., Sylwester, J., Siarkowski, M., et al. 2019, SoPh, 294, 176

Sylwester, J., Kowalinski, M., Gburek, S., et al. 2010, EOSTr, 91, 73

Sylwester, J., Kuzin, S., Kotov, Y., Farnik, F., & Reale, F. 2008, JApA, 29, 339

Tajfirouze, E., & Safari, H. 2012, ApJ, 744, 113

Terzo, S., Reale, F., Miceli, M., et al. 2011, ApJ, 736, 111

Torrence, C., & Compo, G. P. 1998, BAMS, 79, 61

Tripathi, D. 2021, ApJ, 909, 105

Tripathi, D., Nived, V. N., & Solanki, S. K. 2021, ApJ, 908, 28

Upendran, V., & Tripathi, D. 2021a, ApJ, 916, 59

Upendran, V., & Tripathi, D. 2021b, ApJ, 922, 112

Upendran, V., & Tripathi, D. 2022, ApJ, 926, 138

Vadawale, S. V., Mondal, B., Mithun, N. P. S., et al. 2021a, ApJL, 912, L12

Vadawale, S. V., Mithun, N. P. S., Mondal, B., et al. 2021b, ApJL, 912, L13

Vadawale, S. V., Shanmugam, M., Acharya, Y. B., et al. 2014, AdSpR, 54, 2021

van der Walt, S., Colbert, S. C., & Varoquaux, G. 2011, CSE, 13, 22

Vekstein, G. 2009, A&A, 499, L5

Virtanen, P., Gommers, R., Oliphant, T. E., et al. 2020, NatMe, 17, 261

Withbroe, G. L., & Noyes, R. W. 1977, ARA&A, 15, 363

Zhang, P., & Liu, S.-M. 2015, ChA&A, 39, 330